Chemical Engineering Journal 529 (2026) 173060

Contents lists available at ScienceDirect

Chemical Engineering Journal

journal homepage: www.elsevier.com/locate/cej

Oxygen vacancy engineering of $Co_{0.8}Ni_{0.2}Ce_{0.18}Al_{1.4}O_x$ for highly efficient dry reforming of methane enabled by magnetic induction heating

Jianhao Chen, Zhao Li, Zhiyang Yu, Hao-Fan Wang, Yonghai Cao, Hongjuan Wang, Hao Yu *

School of Chemistry and Chemical Engineering, Guangdong Provincial Key Lab of Green Chemical Product Technology, South China University of Technology, Guangzhou, 510641, China

ARTICLE INFO

Keywords:
Dry reforming of methane
Magnetic induction heating
Oxygen vacancies
Coke resistance
Electrification

ABSTRACT

The dry reforming of methane (DRM) provides a promising pathway to the co-conversion of CH_4 and CO_2 into syngas. However, its large-scale deployment remains hindered by severe carbon deposition as well as the high energy consumption and additional CO_2 emissions associated with heating powered by fossil fuels. In this work, we prepared a Ce-doped CoNiAl spinel catalyst ($Co_{0.8}Ni_{0.2}Ce_{0.18}Al_{1.4}O_x$) via the sol–gel method, which exhibits excellent activity and stability for DRM under magnetic induction heating (MIH) powered by electricity. The incorporation of Ce induces the formation of abundant oxygen vacancies, effectively suppressing carbon accumulation and facilitating CO_2 activation. Compared to conventional resistance furnace heating, MIH enables rapid volumetric heating up to about 400 °C min^{-1}, reducing startup energy consumption by an order of magnitude. The optimized catalyst demonstrates remarkable coke resistance, and maintains stable performance over 100 on/off cycles, highlighting its compatibility with intermittent renewable power. This study underscores the critical role of oxygen vacancies in tuning catalytic performance and establishes MIH as an efficient electrification strategy for high-temperature catalytic processes.

1. Introduction

Achieving the global "dual carbon" targets requires a fundamental transformation of the energy system, including large-scale decarbonization, deep integration of renewable energy, and the reduction and valorization of greenhouse gas emissions [1–3]. Among the various carbon utilization strategies, the dry reforming of methane (DRM) enables the direct conversion of two major greenhouse gases—methane (CH_4) and carbon dioxide (CO_2)—into syngas, a mixture of H_2 and CO with significant industrial value [4–6]. This process offers flexible tunability of the H_2/CO ratio, making it particularly suitable for downstream processes with stringent syngas composition requirements, such as Fischer–Tropsch synthesis [7] or alcohol production [8].

$$CH_4 + CO_2 \rightarrow 2CO + 2H_2 \quad (\Delta H^{\ominus}_{298} = 247.3 \text{ kJ mol}^{-1}) \tag{1}$$

However, the large-scale industrial implementation of DRM is primarily constrained by two major challenges: catalyst coking and high energy demand [9–11]. First, carbon deposited during the reaction may cover active sites, block catalyst pores, and increase reactor pressure drop [12]. Coke formation mainly originates from the direct decomposition of methane into amorphous carbon [13] and the Boudouard reaction ($2CO \rightarrow C + CO_2$), which produces graphitic carbon [14] and typically accumulates continuously on metal sites. To address this issue, various strategies have been developed, such as constructing intermetallic compounds [15], strengthening metal–support interactions [16], and minimizing metal particle size [17]. Nevertheless, carbon deposition remains a persistent challenge. Second, DRM is highly endothermic ($\Delta H = 247.3$ kJ mol^{-1}), operated at elevated temperatures above 700 °C [18]. Conventional heating relies on fossil fuel combustion, resulting in both high energy consumption and significant additional CO_2 emissions [19], which is fundamentally incompatible with the goal of carbon neutrality. Consequently, the development of electrified heating strategies powered by renewable energy is urgently needed.

Magnetic induction heating (MIH) is an emerging electrified catalytic heating technology that converts the energy of an alternating electromagnetic field directly into localized thermal energy within the catalyst [20]. Unlike conventional heating, which relies on heat transfer and convection from the reactor walls, MIH generates heat in situ through three primary mechanisms: (1) magnetic hysteresis losses of ferromagnetic materials [21], (2) relaxation losses of

* Corresponding author.
E-mail address: yuhao@scut.edu.cn (H. Yu).

https://doi.org/10.1016/j.cej.2026.173060
Received 27 October 2025; Received in revised form 30 December 2025; Accepted 14 January 2026
Available online 18 January 2026
1385-8947/© 2026 Elsevier B.V. All rights are reserved, including those for text and data mining, AI training, and similar technologies.

superparamagnetic nanoparticles [22], (3) eddy current (Joule) heating [23], where alternating magnetic fields induce circulating currents in conductive components that dissipate energy as heat. These mechanisms enable highly efficient volumetric heating. Because MIH provides direct, bulk heating without preheating reactor walls or large external media, it allows ultrafast heating rates and precise dynamic temperature control [24]. More importantly, MIH can be directly powered by renewable electricity, offering a pathway to decouple high-temperature catalytic processes from fossil fuel dependence.

In recent years, MIH technology has been preliminarily explored in several reaction systems, including CO_2 methanation [20,25–27], steam reforming of methane [28], Fischer–Tropsch synthesis [29], and the degradation of organic pollutants [30]. However, its application in DRM remains relatively limited [31–33]. For highly endothermic reactions such as DRM, the effectiveness of MIH strongly depends on the intrinsic properties of the catalyst, as heat generation is directly associated with magnetically responsive and electrically conductive components. Under such conditions, catalyst design for MIH-driven DRM requires the simultaneous integration of multiple functionalities [34], including efficient magnetothermal conversion, high catalytic activity for CH_4 and CO_2 activation, and resistance to carbon deposition. In particular, the spatial proximity between heat-generating phases, active metal sites, and oxygen-vacancy-rich domains is expected to play a critical role in governing reactivity and coke evolution. However, most existing DRM catalysts have been developed primarily for conventional heating environments, and how oxygen vacancy engineering and metal–support interactions should be tailored to meet the combined requirements of catalytic activity and magnetothermal performance remains poorly understood. Ni-based catalysts have demonstrated industrial potential for DRM due to their favorable activity and cost advantages [35]. Nevertheless, the relatively low Curie temperature (Tc = 358 °C) of Ni severely limits its effectiveness as a heating component under MIH, especially for reactions operating above 700 °C. This constraint highlights the necessity of incorporating alternative ferromagnetic phases and defect-engineered oxide supports to achieve both efficient heating and stable catalytic performance under MIH conditions.

In this work, we synthesized a Ce-doped CoNiAl spinel catalyst ($Co_{0.8}Ni_{0.2}Ce_{0.18}Al_{1.4}O_x$) via the sol–gel method for DRM driven by MIH. Ce doping effectively increased the concentration of surface oxygen vacancies, thereby promoting CO_2 activation and substantially suppressing carbon deposition. Meanwhile, the CoNi alloy phase endowed the catalyst with great magnetothermal properties, enabling the DRM reaction above 700 °C under an applied magnetic field of 7.7 mT. Compared to conventional resistance furnace heating (RFH), MIH exhibited remarkable energy efficiency advantages. Beyond elucidating the critical role of oxygen vacancies in DRM, this work also provides a feasible materials design and system integration strategy for advancing efficient and electrified high-temperature catalytic processes.

2. Experimental section

2.1. Synthesis of $Co_xNi_{1-x}Ce_yAl_zO_4$ catalysts

The $Co_xNi_{1-x}Ce_yAl_zO_4$ catalyst was synthesized via a sol–gel method using citric acid ($C_6H_8O_7$) as the chelating agent. Metal nitrates were employed as precursors: 0.02 mol cobalt (II) nitrate hexahydrate ($Co(NO_3)_2{\cdot}6H_2O$), 0.005 mol nickel(II) nitrate hexahydrate ($Ni(NO_3)_2{\cdot}6H_2O$), together with the required amount of cerium(III) nitrate hexahydrate ($Ce(NO_3)_3{\cdot}6H_2O$) and aluminum nitrate nonahydrate ($Al(NO_3)_3{\cdot}9H_2O$), were dissolved in deionized water to obtain a homogeneous precursor solution. Citric acid was subsequently added with a molar ratio of citric acid to total metal ions of 1:1. The solution was heated in a water bath at 80 °C under continuous stirring until a viscous gel was formed. The obtained gel was dried at 110 °C for 12 h in an oven and then calcined in air at 800 °C for 5 h with a heating rate of 10 °C min^{-1} to afford the $Co_xNi_{1-x}Ce_yAl_zO_4$ solid powder.

2.2. Synthesis of $Co_{0.8}Ni_{0.2}@Al_2O_3$/IMP

For comparison, the $Co_{0.8}Ni_{0.2}@Al_2O_3$/IMP catalyst was prepared by an impregnation method. Typically, 1.433 g $Co(NO_3)_2{\cdot}6H_2O$ and 0.347 g $Ni(NO_3)_2{\cdot}6H_2O$ were dissolved in 10 mL deionized water to form a clear precursor solution, into which 1 g of γ-Al_2O_3 support was introduced. The suspension was stirred thoroughly for 12 h, followed by complete drying using a freeze dryer. The dried powder was subsequently calcined in air at 800 °C for 5 h with a heating rate of 10 °C min^{-1} to yield the $Co_{0.8}Ni_{0.2}@Al_2O_3$/IMP solid powder.

2.3. Catalyst characterizations

Powder X-ray diffraction (XRD) patterns were collected on a PANalytical X'pert Powder diffractometer (Netherlands/Germany) using Cu Kα radiation in the 2θ range of 10–80°. The morphology of the samples was examined by field-emission scanning electron microscopy (FESEM, Merlin, Zeiss, Germany). Transmission electron microscopy (TEM, JEM-2100F, JEOL) equipped with an energy-dispersive X-ray spectrometer (EDS) was employed to analyze the elemental composition. The surface chemical states were determined by X-ray photoelectron spectroscopy (XPS, Thermo-VG Scientific Escalab 250Xi). X-ray absorption fine structure (XAFS) spectra were measured on a Rapid XAFS HE Ultra spectrometer (Anhui Absorption Spectroscopy Instrument Co., Ltd.) in transmission mode at 20 kV and 20 mA. Temperature-programmed reduction (H_2-TPR) and CO_2 temperature-programmed desorption (CO_2-TPD) experiments were carried out on an AutoChem II 2920 automated chemisorption analyzer (Micromeritics) equipped with an in situ thermal conductivity detector (TCD) to quantify H_2 consumption and CO_2 desorption, respectively. CO_2 temperature-programmed surface reaction (CO_2-TPSR) experiments were carried out on an AutoChem III (Micromeritics) equipped with a Cirrus 3 mass spectrometer. The reduced samples were exposed to 30 mL/min 5% CO_2/He and then ramped to 1073 K with a heating rate of 10 °C min^{-1}. Thermogravimetric analysis (TGA) of the spent catalysts was performed on a STA 449C thermal analyzer (Netzsch) to determine the amount of carbon deposition during the DRM reaction. Raman spectroscopy (LabRAM Odyssey, Horiba Jobin-Yvon) was employed to identify the nature of deposited carbon species on the used catalysts. Electron paramagnetic resonance (EPR) spectra were obtained on a Bruker EMX Plus spectrometer. The electricity consumption was directly measured using a power meter connected in series with the power supply of the heating system. Both the induction heating device and the conventional resistance furnace were connected to the same power meter to ensure consistent measurement criteria.

The magnetic properties were evaluated by vibrating sample magnetometry (VSM, LakeShore 7404) at 303 K in the magnetic field range of −2 to 2 T, with a sensitivity of 5×10^{-7} emu. The heating ability of the magnetic nanoparticles was expressed as the specific loss power (SLP), measured on a custom-built magnetic induction heating device (model SPG-06-I). The SLP value was calculated according to Eq. (2): [30].

$$SLP = Cp\ ,\ s\ \frac{\Delta T}{\Delta t}\frac{m_s}{m_{magn}} \tag{2}$$

where $C_{p,s}$ is the specific heat capacity of the solution, approximated as that of water (4.18 J g^{-1} K^{-1}), $\Delta T/\Delta t$ is the initial temperature change rate of the solution, m_s is the total solution mass, approximated as the mass of water, and m_{magn} is the mass of magnetic catalyst. The device operated at a frequency of 300 kHz with a maximum central magnetic field intensity of 4.8 kA m^{-1}. For the measurements, 25 mg of catalyst was dispersed in 5 mL deionized water and placed in a vacuum Dewar vessel positioned at the center of the coil. A fiber optic probe was inserted into the bottom of the solution to monitor the temperature. After 2 min of magnetic induction heating, the subsequent cooling

profile was recorded. To ensure reliability, three consecutive "on–off–on" MIH cycles were conducted, and the average SLP value was obtained from the three measurements.

2.4. Catalytic performance evaluation under resistance furnace heating

The DRM reaction was carried out in a quartz tubular reactor with an inner diameter of 8 mm. Prior to the experiment, 100 mg of catalyst powder was loaded in the middle of the reactor and fixed with quartz wool on both sides. Pure N_2 was first introduced into the reactor to remove residual air. Subsequently, the reactor was heated from room temperature to 800 °C at a rate of 10 °C·min^{-1} under a 100 mL·min^{-1} flow of 20% H_2/N_2 and maintained for 2 h to reduce the catalyst. After the reduction, the gas flow was switched to pure N_2 for reactor purging. The feed gas mixture with a volumetric ratio of CH_4:CO_2:N_2 = 1:1:2 was then introduced into the reactor at a total flow rate of 60 mL·min^{-1}, corresponding to a gas hourly space velocity (GHSV) of 36,000 mL·h^{-1}·g_{cat}^{-1}. The inlet and outlet concentrations of CH_4, CO_2, H_2, and CO were analyzed using an online gas chromatograph (GC 9790, Fuli, China). Long-term stability tests were also performed under identical conditions.

The conversions of CH_4 and CO_2 were calculated according to the following equations [36]:

$$CH_4\ \text{conversion} = X_{CH_4}(\%) = \frac{F_{CH_4}^{in} - F_{CH_4}^{out}}{F_{CH_4}^{in}} \times 100\%$$

$$CO_2\ \text{conversion} = X_{CO_2}(\%) = \frac{F_{CO_2}^{in} - F_{CO_2}^{out}}{F_{CO_2}^{in}} \times 100\%$$

$$\frac{H_2}{CO} = \frac{F_{H_2}^{out}}{F_{CO}^{out}}$$

where $F_{CH_4}^{in}$ and $F_{CO_2}^{in}$ represent the inlet molar flow rates of CH_4 and CO_2, respectively, while $F_{CH_4}^{out}$, $F_{CO_2}^{out}$, $F_{H_2}^{out}$ and F_{CO}^{out} correspond to the outlet molar flow rates of CH_4, CO_2, H_2, and CO, respectively.

2.5. Catalytic performance evaluation under magnetic induction heating

Similar to the resistance furnace heating experiments, the DRM reaction under magnetic induction heating (MIH) was carried out in a quartz tubular reactor with an inner diameter of 8 mm. The experimental setup is schematized in Fig. S1. Prior to the experiment, 300 mg of catalyst powder was loaded in the middle of the reactor and fixed with quartz wool on both sides. Pure N_2 was first introduced to remove residual air. The reactor was then heated from room temperature to 800 °C at a rate of 10 °C·min^{-1} under a 100 mL·min^{-1} flow of 20% H_2/N_2 and

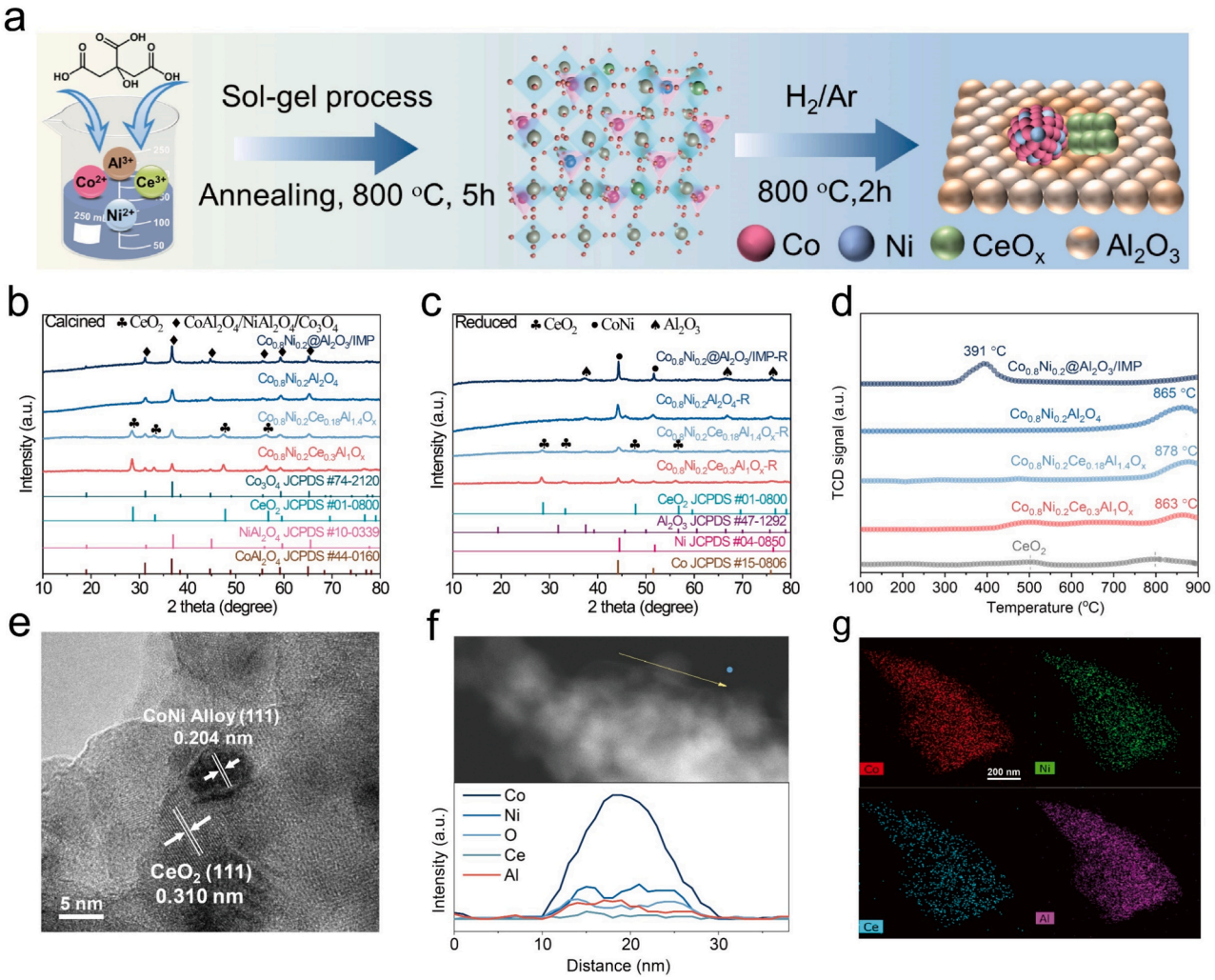

Fig. 1. (a) Schematic illustration of the synthesis of $Co_xNi_{1-x}Ce_yAl_zO_4$ catalysts. (b) XRD patterns of the catalysts after calcination. (c) XRD patterns of the catalysts after reduction. (d) H_2-TPR profiles of the calcined catalysts. (e) HRTEM image of the reduced $Co_{0.8}Ni_{0.2}Ce_{0.18}Al_{1.4}O_x$ catalyst. (f) HAADF-STEM image and the corresponding elemental line scan profile. (g) EDS spectra of the catalyst.

maintained for 2 h to reduce the catalyst. After reduction, the gas flow was switched to pure N_2 to purge the reactor. Subsequently, the reactor was transferred to a high-frequency magnetic field generator for MIH. The alternating magnetic field was generated by an 8-turn water-cooled hollow copper coil with an inner diameter of 3 cm, operating at a fixed frequency of 300 kHz. The gas-phase feed mixture (CH_4:CO_2:N_2 = 1:1:2) was passed through the reactor at a total flow rate of 60 mL·min^{-1}, corresponding to a gas hourly space velocity (GHSV) of 12,000 mL·h^{-1}·g_{cat}^{-1}.

3. Results and discussion

3.1. Synthesis of magnetic CoNi alloy catalysts

$Co_xNi_{1-x}Ce_yAl_zO_4$ catalysts were synthesized via a sol–gel method, as illustrated in Fig. 1a. As shown in Fig. 1b, the calcined catalysts with various Ce content exhibit distinct diffraction peaks at 2θ = 31.1°, 36.7°, 44.6°, 59.1°, and 65.0°, which are characteristic of spinel-type oxide structures spinel phases. Owing to the strong overlap of diffraction peaks among $CoAl_2O_4$, $NiAl_2O_4$, and Co_3O_4 phases, these reflections are indicative of Co–Al–O-based spinel-like structures rather than allowing unambiguous assignment to a single stoichiometric phase, which is demonstrated by the intensity ratio of the main and secondary peaks. Additional diffraction peaks at 2θ = 28.6°, 33.2°, 47.8°, 56.7°, and 59.5° appear in the Ce-doped samples, corresponding to the characteristic signals of CeO_2. Meanwhile, the intensity of the Co and Ni spinel peaks decreases upon Ce doping, indicating partial substitution of Al by Ce [37]. In contrast, the $Co_{0.8}Ni_{0.2}$@Al_2O_3/IMP catalyst prepared by the impregnation method shows prominent Co_3O_4 diffraction peaks at 2θ = 31.2°, 36.7°, 44.7°, 59.3°, and 65.1°. After reduction, characteristic peaks appear at 2θ = 44.2°, 51.5°, and 75.8°, corresponding to the (111), (200), and (220) planes of metallic Co, Ni, or CoNi alloys (Fig. 1c). A series of $Co_xNi_{1-x}Al_2O_4$ samples with varying Co/Ni ratios were also synthesized. As shown in Fig. S2, the diffraction peaks of $Co_xNi_{1-x}Al_2O_4$ samples lie between those of pure Ni and pure Co, gradually shifting to lower angles with increasing Co content. This trend is attributed to the larger atomic radius of Co relative to Ni, providing further evidence for alloy formation between the two metals. Notably, the CeO_2-related diffraction peaks are significantly weakened after reduction, suggesting partial reduction of CeO_2 and the possible formation of a mixed Ce^{3+}/Ce^{4+} phase.

H_2-TPR measurements were conducted for probing the metal–support interaction (MSI). As shown in Fig. 1d, all the spinel-based catalysts prepared via the sol–gel method exhibited reduction peaks above 800 °C in the temperature range of 100–900 °C, which are attributed to the reduction of Co and Ni species in the spinel structure. In contrast, the $Co_{0.8}Ni_{0.2}$@Al_2O_3/IMP catalyst prepared by impregnation showed a reduction peak at 391 °C, indicating the weak MSI. Moreover, the $Co_{0.8}Ni_{0.2}Al_2O_4$ catalyst displayed only one reduction peak at 865 °C, whereas the Ce-doped samples exhibited a minor reduction peaks at 501 °C, likely due to hydrogen consumption by the partial reduction of CeO_2. Among the spinel catalysts, $Co_{0.8}Ni_{0.2}Ce_{0.18}Al_{1.4}O_x$ shows the highest reduction temperature, suggesting that an appropriate amount of Ce dopants enhance the MSI [38].

Fig. 1e shows the high-resolution transmission electron microscopy (HRTEM) image of the reduced $Co_{0.8}Ni_{0.2}Ce_{0.18}Al_{1.4}O_x$ catalyst. The (111) lattice planes of CeO_2 and the CoNi alloy can be clearly observed, with the CoNi alloy closely interfaced with CeO_2. High-angle annular dark-field scanning transmission electron microscopy (HAADF-STEM) imaging and the corresponding elemental line scan profile (Fig. 1f) reveal overlapping signals of Co and Ni, further confirming the formation of the CoNi alloy. EDS elemental mapping (Fig. 1g) indicates a uniform distribution of Co, Ni, Al, and Ce throughout the catalyst.

The magnetic properties of the catalysts, including saturation magnetization (M_s) and coercivity (H_c), were measured at room temperature using a vibrating sample magnetometer (VSM). As shown in Fig. 2a, catalysts with varied molar ratio of Co and Ni exhibit typical ferromagnetic behavior at room temperature. The coercivity of the catalysts progressively decreased with increasing Ni content. The highest saturation magnetization was achieved at Co:Ni molar ratios of 4:1

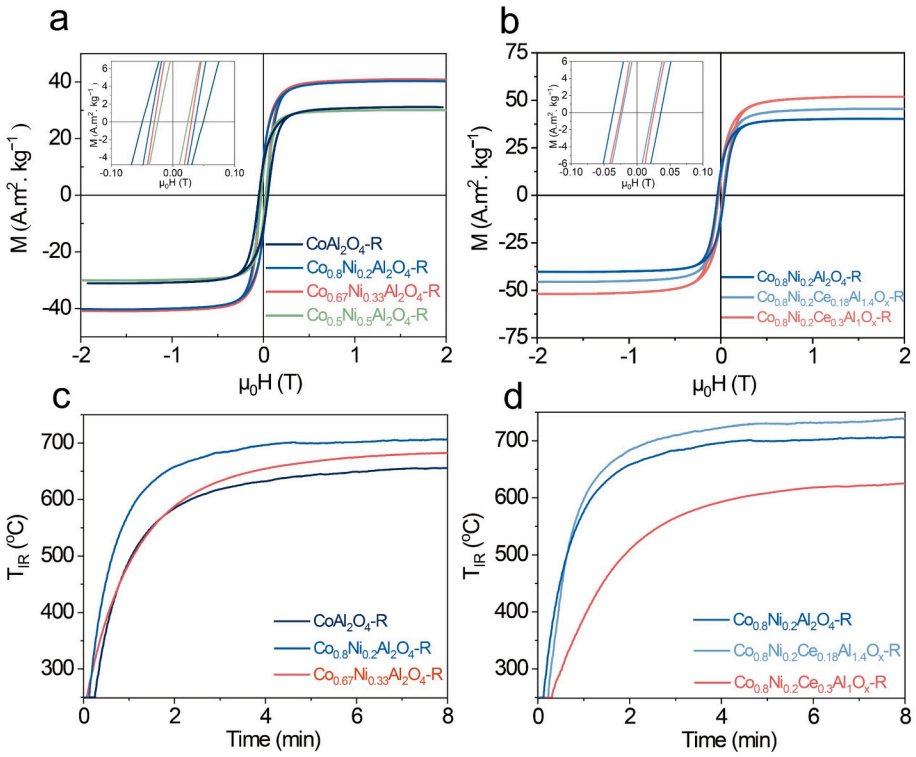

Fig. 2. M–H hysteresis loops measured at 300 K of (a) $Co_xNi_{1-x}Al_2O_4$ and (b) $Co_{0.8}Ni_{0.2}Ce_yAl_zO_x$. The insets show the corresponding magnified views. Induction heating profiles of (c) $Co_xNi_{1-x}Al_2O_4$ and (d) $Co_{0.8}Ni_{0.2}Ce_yAl_zO_x$ under 7.70 mT.

and 2:1. Although the Co:Ni = 1:0 sample exhibited the highest coercivity, its relatively low saturation magnetization would limit efficient energy release through hysteresis loss. To avoid interference from high-frequency magnetic fields on conventional K-type thermocouples, an Optris infrared pyrometer (pH-CTLaser 3 M, wavelength is 2.3 μm) was used for real-time temperature monitoring. The pyrometer was calibrated in advance using a tubular furnace with a visual window to ensure accuracy, the tubes and the visual windows are all made of quartz, having the same material as the reactor tubes. The measured temperature is denoted as T_{IR} (Fig. S3). The magnetic heating capability was further evaluated under a fixed magnetic field of 7.7 mT (Fig. 2c). The $Co_xNi_{1-x}Al_2O_4$ catalyst with a 4:1 Co and Ni molar ratio reached the highest temperature, demonstrating optimal magnetic heating performance among the investigated compositions.

The doping of Ce often introduces more alkaline sites, thereby enhancing the CO_2 activation ability of the catalyst. As shown in Fig. 2b, $Co_{0.8}Ni_{0.2}Ce_{0.18}Al_{1.4}O_x$-R ("R" denotes the catalyst sample after reduction pretreatment in H_2 at 800 °C for 2 h) and $Co_{0.8}Ni_{0.2}Ce_{0.3}Al_1O_x$-R show the higher saturation magnetization than $Co_{0.8}Ni_{0.2}Al_2O_4$-R, which can be attributed to the introduction of soft magnetic components that reduce coercivity and enhance M_s. Calorimetric measurements conducted under an alternating magnetic field (300 kHz, 3.0 mT) are summarized in Figs. S4. Among the tested samples, $Co_{0.8}Ni_{0.2}Ce_{0.3}Al_1O_x$-R shows the worst heating performance, because excessive Ce disrupts Co—Ni metallic connectivity and increases oxide-rich domains, reducing effective magnetic loss pathways and eddy-current [39]. $Co_{0.8}Ni_{0.2}Ce_{0.18}Al_{1.4}O_x$-R delivered the highest specific loss power (SLP) of 37.85 $W{\cdot}g^{-1}$, indicating superior induction heating performance. As displayed in Fig. 2d, $Co_{0.8}Ni_{0.2}Ce_{0.18}Al_{1.4}O_x$-R exhibited an extremely high heating rate of 400–500 °C min^{-1} and the highest temperature at a magnetic field strength of 7.70 mT.

3.2. Oxygen-vacancy enhanced DRM

The DRM performance of $Co_{0.8}Ni_{0.2}Ce_yAl_2O_4$ catalysts was systematically evaluated under resistance furnace heating (RFH). As shown in Fig. 3a and b, the catalytic activity increased significantly with rising temperature, because of the endothermic nature of the DRM reaction. Among all catalysts, $Co_{0.8}Ni_{0.2}Ce_{0.18}Al_{1.4}O_x$-R exhibited the highest CH_4 and CO_2 conversions at all temperatures, reaching 90.2% for CH_4 and 91.4% for CO_2 at 800 °C. The H_2/CO ratio for $Co_{0.8}Ni_{0.2}Ce_{0.18}Al_{1.4}O_x$-R increased from 0.75 at 600 °C to 0.93 at 800 °C (Fig. 3c). For all catalysts, the CO_2 conversion was higher than the CH_4 conversion, and the H_2/CO ratio remained below 1, which can be attributed to the reverse water–gas shift (RWGS) reaction consuming H_2 and generating additional CO (see Fig. S4 for details of equilibrium conversion). Stability tests were further conducted at 700 °C. As Fig. 3d–f depict, the $Co_{0.8}Ni_{0.2}$@Al_2O_3/IMP-R catalyst prepared by impregnation experienced a decline in CH_4 conversion from an initial 62.2% to 44.5% after 10 h, while the undoped $Co_{0.8}Ni_{0.2}Al_2O_4$-R catalyst decreased from 69.1% to 55.0% over the same period. The significant activity loss is mainly due to severe carbon deposition during the reaction, which covered part of the active sites. SEM images (Fig. S5) revealed the formation of substantial filamentous carbon or carbon nanotubes on the spent $Co_{0.8}Ni_{0.2}Al_2O_4$-R catalyst. In contrast, the introduction of Ce notably improved catalytic stability. The $Co_{0.8}Ni_{0.2}Ce_{0.18}Al_{1.4}O_x$-R catalyst showed almost no activity loss after 10 h, and SEM observation indicated no detectable carbon deposition on its surface. Compared with other catalysts reported in literatures (Table S1, Supporting Information), $Co_{0.8}Ni_{0.2}Ce_{0.18}Al_{1.4}O_x$-R demonstrates competitive catalytic activity and stability.

The carbon deposition on the spent catalysts was further evaluated by TGA and Raman spectroscopy. As shown in Fig. 4a, the impregnation-prepared $Co_{0.8}Ni_{0.2}$@Al_2O_3/IMP-R catalyst exhibited a significant weight loss, indicating substantial carbon accumulation on its surface. In contrast, the spinel-derived catalysts $Co_{0.8}Ni_{0.2}Al_2O_4$-R and $Co_{0.8}Ni_{0.2}Ce_{0.3}Al_1O_x$-R showed only minor weight loss, suggesting a lower amount of deposited carbon. Notably, almost no weight loss was observed for the spent $Co_{0.8}Ni_{0.2}Ce_{0.18}Al_{1.4}O_x$-R catalyst, demonstrating that appropriate Ce doping effectively suppresses carbon deposition. Raman spectroscopy further confirmed these findings (Fig. 4b). The $Co_{0.8}Ni_{0.2}$@Al_2O_3/IMP-R catalyst exhibited an I_D/I_G ratio of 0.54, indicative of a relatively refractory coke with high graphitization degree, which can readily lead to deactivation [40]. The sol–gel derived $Co_{0.8}Ni_{0.2}Al_2O_4$-R and $Co_{0.8}Ni_{0.2}Ce_{0.3}Al_1O_x$-R catalysts showed higher I_D/I_G ratios of 0.98 and 0.99, respectively, implying a significant

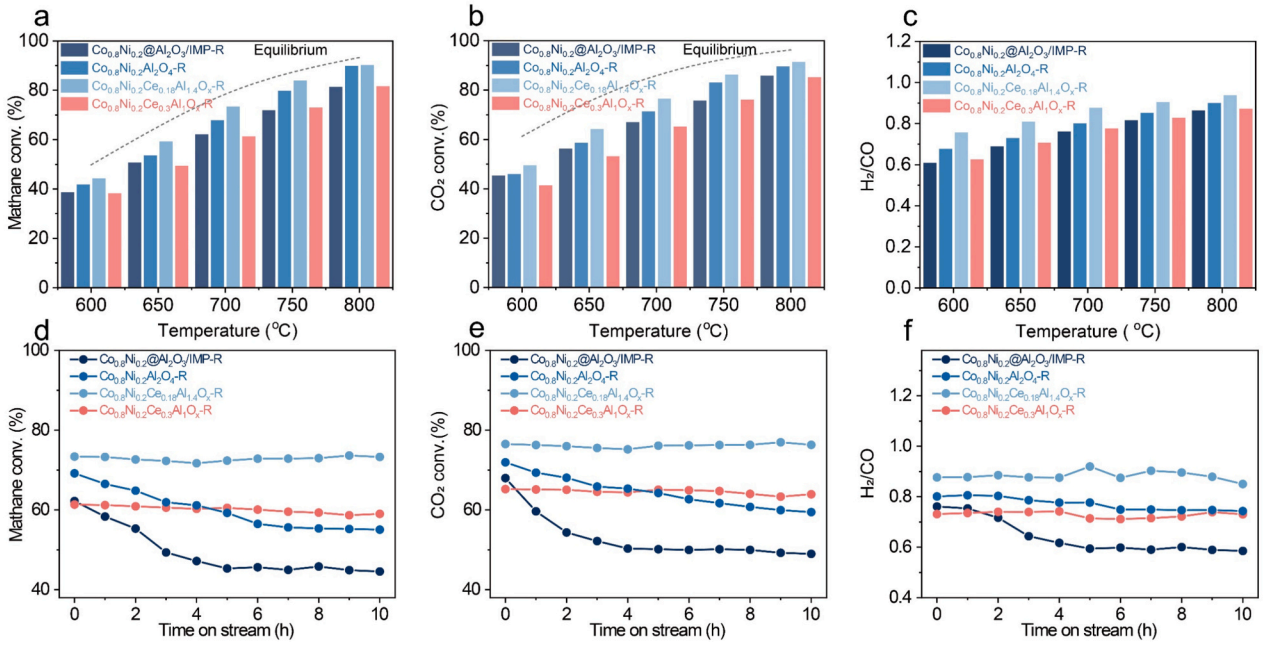

Fig. 3. DRM performances under resistance furnace heating. (a) CH_4 conversion, (b) CO_2 conversion, and (c) H_2/CO molar ratio at temperatures ranging from 600 to 800 °C. (d-f) Stability test of the catalysts showing (d) CH_4 conversion, (e) CO_2 conversion, and (f) H_2/CO molar ratio. Reaction conditions: Resistance furnace heating, 100 mg catalyst, feed gas composition $CH_4/CO_2/N_2$ = 1/1/2, weight hourly space velocity (WHSV) = 36,000 mL g_{cat}^{-1} h^{-1}.

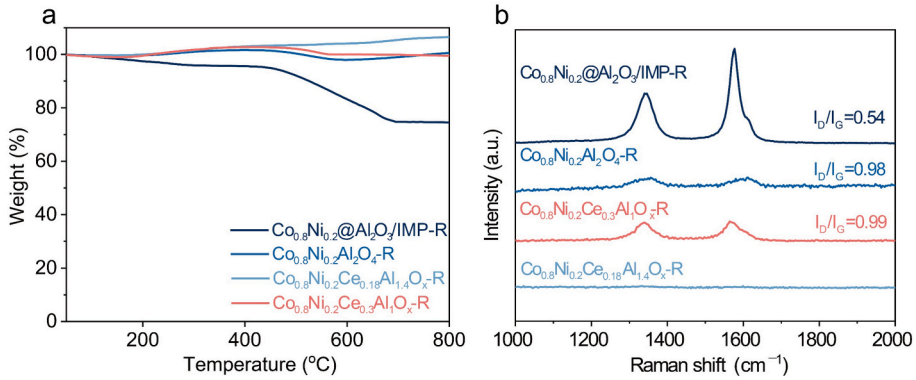

Fig. 4. (a) TGA curves and (b) Raman spectra of the spent catalysts after the stability test.

decrease in the graphitization degree of the deposited carbon. Remarkably, no distinct D and G bands were detected in the Raman spectrum of $Co_{0.8}Ni_{0.2}Ce_{0.18}Al_{1.4}O_x$-R, further confirming its excellent resistance to carbon formation.

To elucidate the origin of the high stability and superior anti-coking performance of the catalysts, CO_2-TPD experiments were conducted to investigate the adsorption and activation behavior of CO_2. According to previous reports [41,42], the CO_2-TPD profiles exhibit three characteristic desorption peaks below 200 °C, between 200 and 350 °C, and above 350 °C, which are assigned to the desorption of weakly adsorbed bicarbonates (associated with surface OH groups), bidentate carbonates formed on medium-strength basic sites (arising from acid–base site interactions), and monodentate carbonates adsorbed on strong basic sites (bound to low-coordination lattice oxygen), respectively. Among these adsorbed species, the weak and medium-strength basic sites are generally considered as the main active centers for CO_2 adsorption and activation. As displayed in Fig. 5a, all catalysts showed three CO_2 desorption peaks. Among these catalysts, $Co_{0.8}Ni_{0.2}Ce_{0.18}Al_{1.4}O_x$-R exhibited the larger total peak area, indicating its stronger CO_2 adsorption capacity.

EPR spectroscopy was employed to detect unpaired electrons associated with defect sites in the selected catalysts. As Fig. 5b depicts, the signal at g = 2.003 can be attributed to oxygen vacancies (O_V) [43,44]. $Co_{0.8}Ni_{0.2}Ce_{0.18}Al_{1.4}O_x$-R displayed the highest intensity of the oxygen vacancy signal, suggesting the highest concentration of oxygen vacancies among all the catalysts. The O 1 s XPS spectra (Fig. 5c) could be deconvoluted into three peaks located at 529.88 eV, 531.58 eV, and 533.08 eV, corresponding to lattice oxygen (O_L), oxygen species adsorbed on O_V, and surface oxygen species (O_{Sur}), respectively [45,46]. $Co_{0.8}Ni_{0.2}Ce_{0.18}Al_{1.4}O_x$-R demonstrated the highest content of oxygen vacancies (Fig. 5c). Combined EPR and XPS results clearly show that the increased concentration of oxygen vacancies promotes the adsorption and activation of CO_2 on $Co_{0.8}Ni_{0.2}Ce_{0.18}Al_{1.4}O_x$-R.

The valence state and coordination environment of Ce in the reduced $Co_{0.8}Ni_{0.2}Ce_{0.18}Al_{1.4}O_x$-R catalyst were investigated using XAFS

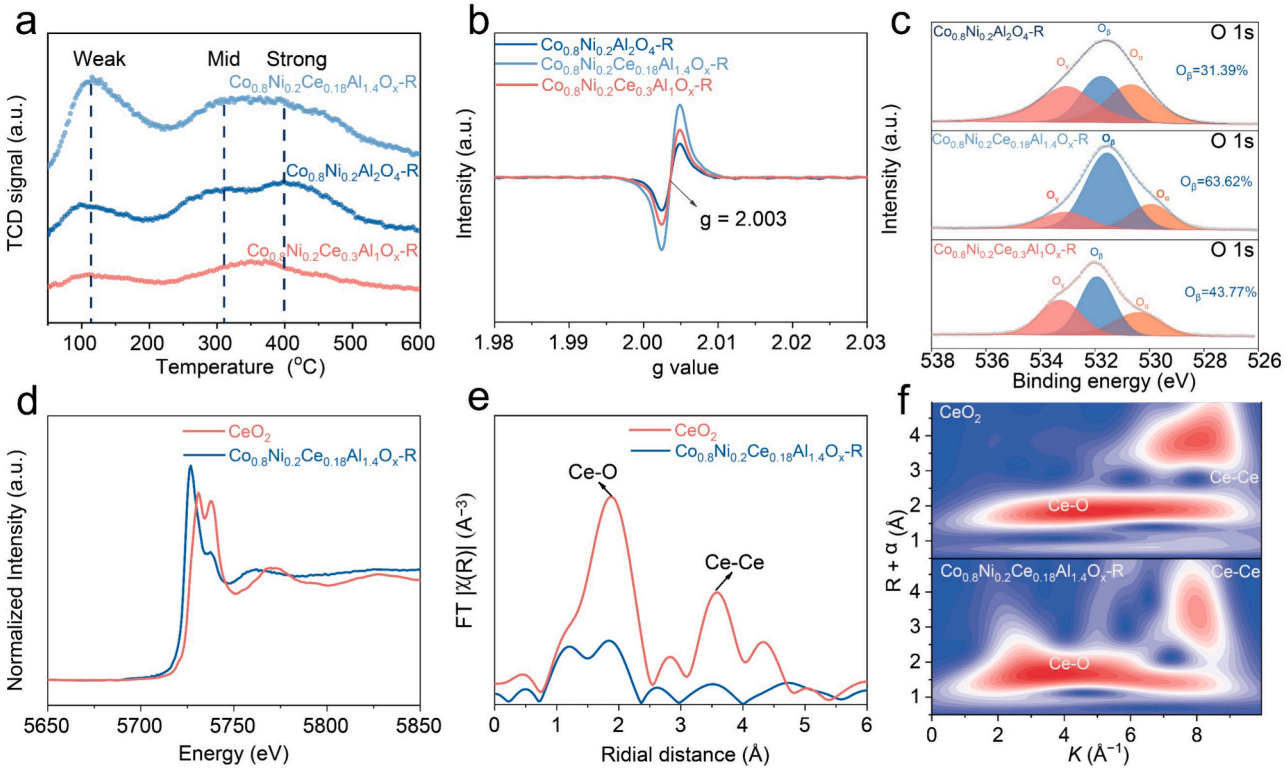

Fig. 5. (a) CO_2-TPD profiles, (b) O 1s XPS spectra, (c) EPR spectra, and (d) Ce L_3-edge X-ray absorption near-edge structure (XANES) spectra of the reduced catalysts with CeO_2 as reference. (e) Fourier-transform EXAFS spectra and (f) corresponding wavelet transform (WT) EXAFS analysis for $Co_{0.8}Ni_{0.2}Ce_{0.18}Al_{1.4}O_x$-R.

spectroscopy. As shown in the Ce L_3-edge XANES spectrum (Fig. 5d), $Co_{0.8}Ni_{0.2}Ce_{0.18}Al_{1.4}O_x$ exhibits a pronounced main absorption peak at approximately 5726.8 eV, accompanied by a weaker feature at 5737.3 eV. This spectral profile distinctly differs from that of the reference CeO_2, which displays two intense peaks at 5731 eV and 5738 eV, indicating an average oxidation state of Ce lower than +4 in the reduced catalyst. In the Fourier-transform extended XAFS (EXAFS) spectrum (Fig. 5e), CeO_2 shows two prominent peaks at 1.87 Å and 3.58 Å, corresponding to the Ce—O and Ce—Ce coordination shells, respectively. In contrast, the intensities of these peaks were significantly reduced for $Co_{0.8}Ni_{0.2}Ce_{0.18}Al_{1.4}O_x$-R, suggesting a decreased coordination number around Ce. Further analysis by EXAFS fitting combined with wavelet transform (WT) provided high-resolution images in k-space and R-space (Fig. 5f). The results reveal that the bond lengths for the first (Ce—O) and the second coordination shell (Ce—Ce) in the catalyst are 1.84 Å and 3.52 Å, respectively, both shorter than those in CeO_2 [47,48]. These findings demonstrate that Ce doping facilitates the formation of less coordinated oxygen species, which can be more readily removed from the lattice to generate oxygen vacancies [47].

Fig. S7 presents the CO_2-TPSR profiles of the reduced catalysts, where the evolution of CO ($m/z = 28$) is employed as a sensitive probe for CO_2 activation. All catalysts exhibit a distinct CO formation signal at elevated temperatures, confirming that CO_2 can be activated and partially dissociated on these surfaces. Notably, the onset temperature for CO evolution follows the order $Co_{0.8}Ni_{0.2}Ce_{0.18}Al_{1.4}O_x$-R < $Co_{0.8}Ni_{0.2}Ce_{0.3}Al_1O_x$-R < $Co_{0.8}Ni_{0.2}Al_2O_4$-R, indicating that the incorporation of an appropriate amount of Ce markedly promotes CO_2 activation. The lowest CO evolution onset temperature observed for $Co_{0.8}Ni_{0.2}Ce_{0.18}Al_{1.4}O_x$-R implies more facile CO_2 activation, which can be directly correlated with its higher concentration of surface oxygen vacancies, as evidenced by EPR analysis. Oxygen vacancies are well known to act as preferential adsorption and activation sites for CO_2, stabilizing carbonate- or bicarbonate-like intermediates and weakening the C—O bonds, thereby enabling CO formation at lower temperatures during TPSR measurements [49]. In contrast, the Ce-free $Co_{0.8}Ni_{0.2}Al_2O_4$-R catalyst exhibits the highest CO formation temperature, reflecting its inferior CO_2 activation capability due to the scarcity of oxygen vacancies. Interestingly, although $Co_{0.8}Ni_{0.2}Ce_{0.3}Al_1O_x$-R contains a higher Ce loading, its CO evolution onset temperature is higher than that of $Co_{0.8}Ni_{0.2}Ce_{0.18}Al_{1.4}O_x$-R, suggesting that excessive Ce addition tends to induce the aggregation of CeO_2 into bulk-like domains, which stabilizes the Ce^{4+} state and reduces the density of surface-accessible oxygen vacancies, leading to a decreased density of accessible oxygen vacancies [50].

3.3. DRM performance under induction heating

Fig. 6 shows the catalytic activity of $Co_{0.8}Ni_{0.2}Ce_yAl_2O_4$ catalysts for DRM under induction heating conditions, along with the corresponding heating temperatures (T_{IR}). As the magnetic field increased, the temperature of all catalysts gradually rose. Owing to the highly endothermic nature of the DRM reaction, the conversions of methane and CO_2 were consequently enhanced. Among them, $Co_{0.8}Ni_{0.2}Ce_{0.18}Al_{1.4}O_x$-R exhibited the highest temperature and DRM activity under the same current, owing to its optimal magnetothermal conversion capability and catalytic performance. At a magnetic field of 5.70 mT, its T_{IR} reached 584 °C, with methane and CO_2 conversions of 89.05% and 89.52%, respectively.

Energy efficiency is of paramount importance for electrified catalytic processes. Induction heating, with its capability for rapid dynamic temperature control, demonstrates significantly superior cold-start performance compared to conventional RFH. As shown in Fig. 7a, the catalyst bed reached the temperature required for 80% methane conversion in only about 4 min. Under fair comparison conditions with identical heating power, the RFH required approximately three times longer to achieve the same conversion, highlighting the notable

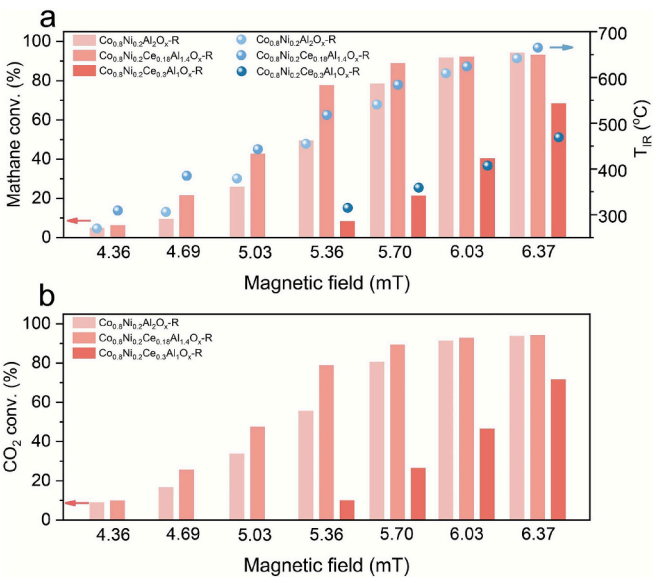

Fig. 6. (a) CH_4 and (b) CO_2 conversions and reactor temperature (T_{IR}) of the catalysts under different magnetic field strengths. Reaction conditions: induction heating, 300 mg catalyst, feed gas composition $CH_4/CO_2/N_2$ = 1/1/2, WHSV = 12,000 mL g_{cat}^{-1} h^{-1}.

intensification in rapid startup.

Fig. 7b further compares the energy consumption of the two heating modes. The MIH consumed only 0.078 kWh of electricity, whereas the RFH required 0.810 kWh, when reaching the reaction temperature required for identical conversion. Under these operating conditions, the energy efficiency of induction heating during the heating phase was approximately 10 times higher than that of the conventional furnace. Therefore, by leveraging the localized and rapid heating characteristics of MIH, this process holds promise for achieving higher overall energy efficiency.

The DRM performance of $Co_{0.8}Ni_{0.2}Ce_{0.18}Al_{1.4}O_x$-R was evaluated under both MIH and RFH under identical conditions (Fig. 7c and d). It is noteworthy that to achieve the same level of methane and CO_2 conversion (80%), the required reaction temperatures under MIH were 288 °C and 258 °C lower than those under RFH, respectively (Fig. 7c and d). At the same apparent reaction temperature, the DRM activity under MIH was nearly an order of magnitude higher than that under RFH. This enhancement can be attributed to the localized heating effect provided by CoNi alloys under alternating magnetic fields, which may create actual reaction temperatures higher than the measured values. These findings align with previously reported enhancement effects of MIH in both liquid-phase and gas-solid catalytic reactions [51–53], highlighting the promise of MIH toward process intensification enabled by fine-tuned magnetic catalysts.

To assess the stability of the MIH DRM system, 100 start-stop cycles (including heating, reaction, and cooling stages) were conducted. As shown in Fig. 7e, both CH_4 and CO_2 conversions remained stable without noticeable degradation throughout the cycling test, while the heating capability of the catalyst was also well maintained. Thermogravimetric analysis performed on the spent $Co_{0.8}Ni_{0.2}Ce_{0.18}Al_{1.4}O_x$-R catalyst after 100 cycles revealed only about 2.0% weight loss (Fig. S7), demonstrating its great coking resistance even after repeated high-conversion operations (with both CH_4 and CO_2 conversions exceeding 90%). Moreover, the catalytic stability of $Co_{0.8}Ni_{0.2}Ce_{0.18}Al_{1.4}O_x$-R was also investigated. As shown in Fig. S9, the conversion of methane and CO_2 remained above 85% after 50 h, further demonstrating its stability under the MIH system. These results confirm the outstanding durability of this catalytic system, highlighting its potential for frequent start-stop operations under intermittent energy supply conditions.

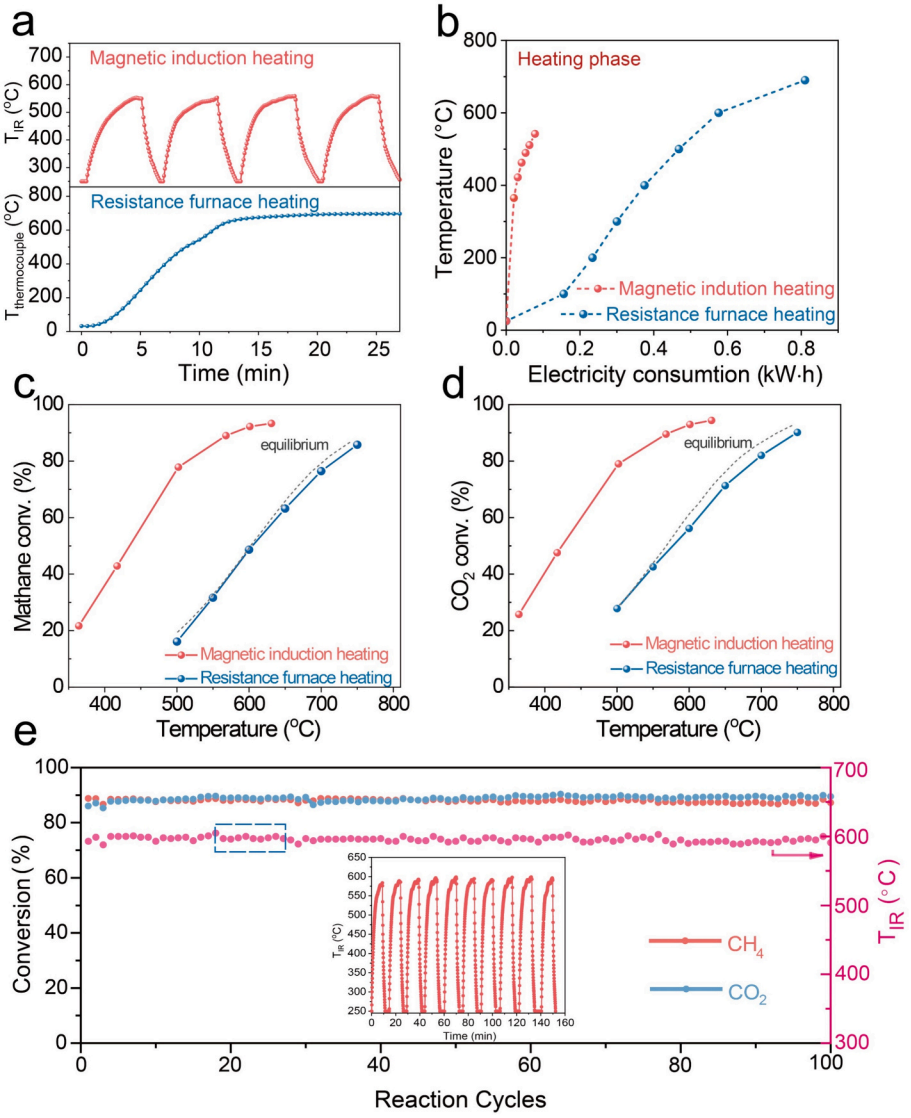

Fig. 7. Performance comparison between magnetic induction heating (MIH) and resistive furnace heating (RFH). (a) Heating rate at identical power input of 1.2 kW. (b) Cold-start energy consumption required to reach 80% CH_4 conversion. (c-d) Comparison of CH_4 and CO_2 conversions. (e) 100 start-stop cycles (including heating, reaction, and cooling stages. The temperature rose from room temperature to approximately 595 °C, and then dropped below 200 °C at the end. Each cycle lasted for about 13 min.) Reaction conditions: 300 mg catalyst, feed gas composition $CH_4/CO_2/N_2 = 1/1/2$, WHSV = 12,000 mL g_{cat}^{-1} h^{-1}.

4. Conclusions

A novel strategy that integrates rational catalyst design with MIH technology opens a promising pathway toward efficient and sustainable DRM. By incorporating Ce into the CoNiAl spinel structure, oxygen vacancies were effectively introduced, which not only promoted CO_2 activation but also significantly suppressed carbon deposition, thereby substantially improving the DRM stability. The high Curie temperature of Co in the $Co_xNi_{1-x}Ce_yAl_zO_4$ catalyst enabled excellent magneto-thermal performance, allowing for rapid and controllable temperature rise under an alternating magnetic field and ensuring highly efficient DRM operation. Compared with RFH, the MIH system reduced the startup energy consumption by approximately 90% and achieved a cold-start transition to high activity within minutes, demonstrating outstanding energy efficiency and dynamic response characteristics. Moreover, the developed catalyst–MIH system exhibited remarkable structural stability and reaction durability over multiple rapid heating–cooling cycles, indicating strong adaptability to intermittent renewable energy supply patterns. In summary, this work not only provides fundamental insights into the critical role of oxygen vacancies in the DRM catalyst but also validates MIH as a highly promising electrification approach for high-temperature catalytic reactions.

CRediT authorship contribution statement

Jianhao Chen: Writing – original draft, Visualization, Investigation, Formal analysis, Data curation. **Zhao Li:** Validation, Data curation. **Zhiyang Yu:** Validation, Data curation. **Hao-Fan Wang:** Supervision, Resources. **Yonghai Cao:** Supervision, Resources. **Hongjuan Wang:** Supervision, Resources. **Hao Yu:** Writing – review & editing, Supervision, Resources, Project administration, Funding acquisition, Conceptualization.

Declaration of competing interest

The authors declare the following financial interests/personal relationships which may be considered as potential competing interests: Hao Yu reports financial support was provided by National Key Research and Development Program of China. Hao Yu reports financial support was provided by the Natural Science Foundation of Guandong Province.

Hao Yu reports financial support was provided by Guizhou Provincial Science and Technology Plan. If there are other authors, they declare that they have no known competing financial interests or personal relationships that could have appeared to influence the work reported in this paper.

Acknowledgements

This work was supported by the Natural Science Foundation of Guandong Province (No. 2024B1515040016) and Guizhou Provincial Science and Technology Plan Project Natural Science Key Project (ZK [2022] 028).

Appendix A. Supplementary data

Supplementary data to this article can be found online at https://doi.org/10.1016/j.cej.2026.173060.

Data availability

Data will be made available on request.

References

[1] J.W. Ager, A.A. Lapkin, Chemical storage of renewable energy, Science 360 (6390) (2018) 707–708, https://doi.org/10.1126/science.aat7918.
[2] A. Islam, S.H. Teo, C.H. Ng, Y.H. Taufiq-Yap, S.Y.T. Choong, M.R. Awual, Progress in recent sustainable materials for greenhouse gas (NO_x and SO_x) emission mitigation, Prog. Mater. Sci. 132 (2023) 101033, https://doi.org/10.1016/j.pmatsci.2022.101033.
[3] C. Graves, S.D. Ebbesen, M. Mogensen, K.S. Lackner, Sustainable hydrocarbon fuels by recycling CO_2 and H_2O with renewable or nuclear energy, Renew. Sust. Energ. Rev. 15 (1) (2011) 1–23, https://doi.org/10.1016/j.rser.2010.07.014.
[4] C. Palmer, D.C. Upham, S. Smart, M.J. Gordon, H. Metiu, E.W. McFarland, Dry reforming of methane catalysed by molten metal alloys, Nat. Catal. 3 (1) (2020) 83–89, https://doi.org/10.1038/s41929-019-0416-2.
[5] Y. Song, E. Ozdemir, S. Ramesh, A. Adishev, S. Subramanian, A. Harale, M. Albuali, B.A. Fadhel, A. Jamal, D. Moon, S.H. Choi, C.T. Yavuz, Dry reforming of methane by stable Ni-Mo nanocatalysts on single-crystalline MgO, Science 367 (6479) (2020) 777–781, https://doi.org/10.1126/science.aav2412.
[6] T. Zhou, X. Li, J. Zhao, L. Luo, Y. Wang, Z. Xiao, S. Hu, R. Wang, Z. Zhao, C. Liu, W. Wu, H. Li, Z. Zhang, L. Zhao, H. Yan, J. Zeng, Ultrafine metal nanoparticles isolated on oxide nano-islands as exceptional sintering-resistant catalysts, Nat. Mater. 24 (6) (2025) 891–899, https://doi.org/10.1038/s41563-025-02134-9.
[7] P.R. Ellis, D.I. Enache, D.W. James, D.S. Jones, G.J. Kelly, A robust and precious metal-free high performance cobalt fischer-tropsch catalyst, Nat. Catal. 2 (7) (2019) 623–631, https://doi.org/10.1038/s41929-019-0288-5.
[8] Q. Gao, J. Xu, J. Wei, J. Yu, Y. Yu, Y. Sun, Q. Ge, J. Sun, Efficient synthesis of alcohols from syngas over Fe_3O_4 modified by P25 and Ca, Appl. Catal. B Environ. 365 (2025) 124995, https://doi.org/10.1016/j.apcatb.2024.124995.
[9] L. He, M. Li, W.-C. Li, W. Xu, Y. Wang, Y.-B. Wang, W. Shen, A.-H. Lu, Robust and coke-free Ni catalyst stabilized by 1-2 nm-thick multielement oxide for methane dry reforming, ACS Catal. 11 (20) (2021) 12409–12416, https://doi.org/10.1021/acscatal.1c02995.
[10] A.V. Tavasoli, M. Preston, G. Ozin, Photocatalytic dry reforming: What is it good for? Energy Environ. Sci. 14 (5) (2021) 3098–3109, https://doi.org/10.1039/d0ee02809f.
[11] A. Tavasoli, A. Gouda, T. Zahringer, Y.F. Li, H. Quaid, C.V.J. Perez, R. Song, M. Sain, G. Ozin, Enhanced hybrid photocatalytic dry reforming using a phosphated Ni-CeO_2 nanorod heterostructure, Nat. Commun. 14 (1) (2023) 1435, https://doi.org/10.1038/s41467-023-36982-3.
[12] K. Bu, S. Kuboon, J. Deng, H. Li, T. Yan, G. Chen, L. Shi, D. Zhang, Methane dry reforming over boron nitride interface-confined and ldhs-derived Ni catalysts, Appl. Catal. B-Environ. 252 (2019) 86–97, https://doi.org/10.1016/j.apcatb.2019.04.007.
[13] H. Xia, C. Dang, D. Zhou, W. Cai, Lamellar cross-linking Ni/CeO_2 as an efficient and durable catalyst for dry reforming of methane, Chem. Eng. J. 489 (2024) 151365, https://doi.org/10.1016/j.cej.2024.151365.
[14] Y. Ye, H. Lei, Y. Qin, Z. Wang, S. Hu, T. Zhou, L. Zhang, R. Wang, Z. Xiao, X. Gao, Q. Ma, S. Shi, H. Zhang, H. Yan, S. Zhou, C. Ma, Z. Liu, J. Tao, J. Zeng, Harmonizing nanoparticle exsolution from Ce-Sm oxide matrix for stable methane dry reforming, Angew. Chem. Int. Ed. 64 (2025) e202503997, https://doi.org/10.1002/anie.202503997.
[15] K.Y. Kim, J.H. Lee, H. Lee, W.Y. Noh, E.H. Kim, E.C. Ra, S.K. Kim, K. An, J.S. Lee, Layered double hydroxide-derived intermetallic $Ni_3GaC_{0.25}$ catalysts for dry reforming of methane, ACS Catal. 11 (17) (2021) 11091–11102, https://doi.org/10.1021/acscatal.1c02200.
[16] Y. Gangarajula, F. Hong, Q. Li, X. Jiang, W. Liu, M. Akri, Y. Su, Y. Zhang, L. Li, B. Qiao, Operando induced strong metal-support interaction of Rh/CeO_2 catalyst in dry reforming of methane, Appl. Catal. B Environ. 343 (2024) 123503, https://doi.org/10.1016/j.apcatb.2023.123503.
[17] P.K. Chaudhary, G. Deo, Influence of particle size and metal-support interaction on the catalytic performance of Ni-Al_2O_3 catalysts for the dry and oxidative-dry reforming of methane, Colloid Surf. A-Physicochem. Eng. Asp. 646 (2022) 128973, https://doi.org/10.1016/j.colsurfa.2022.128973.
[18] J. Yang, Z. Cao, Y. Wan, S. Guan, B. Jiang, Y. Yamauchi, H. Li, Vacancy-anchored sub-nanometer Ru catalyst with high activity and strong durability at 800°C dry reforming of methane, Adv. Energy Mater. 15 (16) (2024) 2404936, https://doi.org/10.1002/aenm.202404936.
[19] R.K. Parsapur, S. Chatterjee, K.-W. Huang, The insignificant role of dry reforming of methane in CO_2 emission relief, ACS Energy Lett. 5 (9) (2020) 2881–2885, https://doi.org/10.1021/acsenergylett.0c01635.
[20] B. Rivas-Murias, J.M. Asensio, N. Mille, B. Rodriguez-Gonzalez, P.-F. Fazzini, J. Carrey, B. Chaudret, V. Salgueirino, Magnetically induced CO_2 methanation using exchange-coupled spinel ferrites in cuboctahedron-shaped nanocrystals, Angew. Chem. Int. Ed. 59 (36) (2020) 15537–15542, https://doi.org/10.1002/anie.202004908.
[21] M. Suto, Y. Hirota, H. Mamiya, A. Fujita, R. Kasuya, K. Tohji, B. Jeyadevan, Heat dissipation mechanism of magnetite nanoparticles in magnetic fluid hyperthermia, J. Magn. Magn. Mater. 321 (10) (2009) 1493–1496, https://doi.org/10.1016/j.jmmm.2009.02.070.
[22] S. Mornet, S. Vasseur, F. Grasset, P. Veverka, G. Goglio, A. Demourgues, J. Portier, E. Pollert, E. Duguet, Magnetic nanoparticle design for medical applications, Prog. Solid State Chem. 34 (2–4) (2006) 237–247, https://doi.org/10.1016/j.progsolidstchem.2005.11.010.
[23] A. Kirschning, L. Kupracz, J. Hartwig, New synthetic opportunities in miniaturized flow reactors with inductive heating, Chem. Lett. 41 (6) (2012) 562–570, https://doi.org/10.1246/cl.2012.562.
[24] W. Wang, G. Tuci, D.-V. Cuong, Y. Liu, A. Rossin, L. Luconi, J.-M. Nhut, N.-D. Lam, P.-H. Cuong, G. Giambastiani, Induction heating: An enabling technology for the heat management in catalytic processes, ACS Catal. 9 (9) (2019) 7921–7935, https://doi.org/10.1021/acscatal.9b02471.
[25] A. Bordet, L.M. Lacroix, P.F. Fazzini, J. Carrey, K. Soulantica, B. Chaudret, Magnetically induced continuous CO_2 hydrogenation using composite iron carbide nanoparticles of exceptionally high heating power, Angew. Chem. Int. Ed. 55 (51) (2016) 15894–15898, https://doi.org/10.1002/anie.201609477.
[26] S.S. Kale, J.M. Asensio, M. Estrader, M. Werner, A. Bordet, D.L. Yi, J. Marbaix, P. F. Fazzini, K. Soulantica, B. Chaudret, Iron carbide or iron carbide/cobalt nanoparticles for magnetically-induced CO_2 hydrogenation over Ni/$SiRAlO_x$ catalysts, Cat. Sci. Technol. 9 (10) (2019) 2601–2607, https://doi.org/10.1039/c9cy00437h.
[27] D. De Masi, J.M. Asensio, P.F. Fazzini, L.M. Lacroix, B. Chaudret, Engineering iron-nickel nanoparticles for magnetically induced CO_2 methanation in continuous flow, Angew. Chem. Int. Ed. 59 (15) (2020) 6187–6191, https://doi.org/10.1002/anie.201913865.
[28] M.R. Almind, S.B. Vendelbo, M.F. Hansen, M.G. Vinum, C. Frandsen, P. M. Mortensen, J.S. Engbaek, Improving performance of induction-heated steam methane reforming, Catal. Today 342 (2020) 13–20, https://doi.org/10.1016/j.cattod.2019.05.005.
[29] A. Meffre, B. Mehdaoui, V. Connord, J. Carrey, P.F. Fazzini, S. Lachaize, M. Respaud, B. Chaudret, Complex nano-objects displaying both magnetic and catalytic properties: A proof of concept for magnetically induced heterogeneous catalysis, Nano Lett. 15 (5) (2015) 3241–3248, https://doi.org/10.1021/acs.nanolett.5b00446.
[30] J. Chen, H. Liu, F. Wang, H.-F. Wang, Y. Cao, H. Wang, X. Yang, H. Yu, Iron-encapsulated carbon nanotubes catalyze degradation of organic pollutants enabled by magnetic induction heating, Carbon 218 (2024) 118746, https://doi.org/10.1016/j.carbon.2023.118746.
[31] F. Varsano, M. Bellusci, A. La Barbera, M. Petrecca, M. Albino, C. Sangregorio, Dry reforming of methane powered by magnetic induction, Int. J. Hydrog. Energy 44 (38) (2019) 21037–21044, https://doi.org/10.1016/j.ijhydene.2019.02.055.
[32] F. Varsano, M. Bellusci, A. Provino, M. Petrecca, Iop, NiCo as catalyst for magnetically induced dry reforming of methane, 1st International Conference on Functional Materials and Chemical Engineering (ICFMCE), Dubai, U ARAB EMIRATES, 2017.
[33] M.N. Perez-Camacho, J. Abu-Dahrieh, D. Rooney, K. Sun, Biogas reforming using renewable wind energy and induction heating, Catal. Today 242 (2015) 129–138, https://doi.org/10.1016/j.cattod.2014.06.010.
[34] H. Li, C. Dang, G. Yang, Y. Cao, H. Wang, F. Peng, H. Yu, Bi-functional particles for integrated thermo-chemical processes: Catalysis and beyond, Particuology 56 (2021) 10–32, https://doi.org/10.1016/j.partic.2020.12.002.
[35] M. Hosseinpour, T. Moser, B. Kloetzer, S. Penner, Regeneration of Ni-Zr methane dry reforming catalysts in CO_2: Reduction of coking and Ni redispersion, ACS Catal. 15 (4) (2025) 3314–3327, https://doi.org/10.1021/acscatal.4c06230.
[36] K. Liu, F. Xing, Y. Xiao, N. Yan, K.-I. Shimizu, S. Furukawa, Development of a highly stable ternary alloy catalyst for dry reforming of methane, ACS Catal. 13 (6) (2023) 3541–3548, https://doi.org/10.1021/acscatal.2c05488.
[37] S. Qamar, M.N. Akhtar, W. Aleem, Z.U. Rehman, A.H. Khan, A. Ahmad, K. M. Batoo, M. Aamir, Graphene anchored Ce doped spinel ferrites for practical and technological applications, Ceram. Int. 46 (6) (2020) 7081–7088, https://doi.org/10.1016/j.ceramint.2019.11.200.
[38] X. Ding, Y. Yang, Z. Li, P. Huang, X. Liu, Y. Guo, Y. Wang, Engineering a nickel-oxygen vacancy interface for enhanced dry reforming of methane: A promoted effect of CeO_2 introduction into Ni/MgO, ACS Catal. 13 (23) (2023) 15535–15545, https://doi.org/10.1021/acscatal.3c04150.

[39] J. Mazario, S. Ghosh, V. Varela-Izquierdo, L.M. Martinez-Prieto, B. Chaudret, Magnetic nanoparticles and radio frequency induction: From specific heating to magnetically induced catalysis, Chemcatchem 17 (2) (2025) e202400683, https://doi.org/10.1002/cctc.202400683.
[40] D. Qin, L. Cai, S. Zhang, W. Chu, W. Yang, Zinc doping boosts the reactivity and anti-coking ability of cobalt-based catalysts for propane dehydrogenation, ACS Catal. 15 (13) (2025) 11794–11805, https://doi.org/10.1021/acscatal.5c02743.
[41] A.S. Al-Fatesh, M.A. Naeem, A.H. Fakeeha, A.E. Abasaeed, Role of La_2O_3 as promoter and support in Ni/γ-Al_2O_3 catalysts for dry reforming of methane, Chin. J. Chem. Eng. 22 (1) (2014) 28–37, https://doi.org/10.1016/s1004-9541(14)60029-x.
[42] C. Italiano, J. Llorca, L. Pino, M. Ferraro, V. Antonucci, A. Vita, CO and CO_2 methanation over Ni catalysts supported on CeO_2, Al_2O_3 and Y_2O_3 oxides, Appl. Catal. B-Environ. 264 (2020) 118494, https://doi.org/10.1016/j.apcatb.2019.118494.
[43] J. Ye, L. Liang, N. Li, W. Gao, X. Xu, Z. Cheng, B. Yan, G. Chen, Oxygen vacancy mediated oxidative reforming of polylactic acid to hydrocarbon, Appl. Catal. B Environ. 375 (2025) 125413, https://doi.org/10.1016/j.apcatb.2025.125413.
[44] W. Zhang, L. Cai, S. Cao, L. Qiao, Y. Zeng, Z. Zhu, Z. Lv, H. Xia, L. Zhong, H. Zhang, X. Ge, J. Wei, S. Xi, Y. Du, S. Li, X. Chen, Interfacial lattice-strain-driven generation of oxygen vacancies in an aerobic-annealed TiO_2(b) electrode, Adv. Mater. 31 (52) (2019) 1906156, https://doi.org/10.1002/adma.201906156.
[45] Q. Wang, C. Yang, S. Zhu, Y. Zhang, X. Wang, Y. Li, W. Ding, X. Guo, Interface engineering of oxygen-vacancy-rich MgO/Ni@NiAlO enables low-temperature coke-free methane dry reforming, Chin. J. Catal. 75 (2025) 9–20, https://doi.org/10.1016/s1872-2067(25)64743-7.
[46] H. Wang, G. Cui, H. Lu, Z. Li, L. Wang, H. Meng, J. Li, H. Yan, Y. Yang, M. Wei, Facilitating the dry reforming of methane with interfacial synergistic catalysis in an Ir@CeO_{2-x} catalyst, Nat. Commun. 15 (1) (2024) 3765, https://doi.org/10.1038/s41467-024-48122-6.
[47] X. Wang, R. Duan, Z. Li, M. Gao, Y. Fu, Y. Han, G. He, H. He, The critical role of oxygen vacancies in N_2O decomposition over cobalt-doped CeO_2 catalysts, Environ. Sci. Technol. 59 (11) (2025) 5839–5847, https://doi.org/10.1021/acs.est.5c00180.
[48] X.-P. Yang, Z.-Z. Wu, Y.-C. Li, S.-P. Sun, Y.-C. Zhang, J.-W. Duanmu, P.-G. Lu, X.-L. Zhang, F.-Y. Gao, Y. Yang, Y.-H. Wang, P.-C. Yu, S.-K. Li, M.-R. Gao, Atomically dispersed cerium on copper tailors interfacial water structure for efficient CO-to-acetate electroreduction, Nat. Commun. 16 (1) (2025) 2811, https://doi.org/10.1038/s41467-025-58109-6.
[49] F. Xing, J. Ma, K.-I. Shimizu, S. Furukawa, High-entropy intermetallics on ceria as efficient catalysts for the oxidative dehydrogenation of propane using CO_2, Nat. Commun. 13 (1) (2022) 5065, https://doi.org/10.1038/s41467-022-32842-8.
[50] C. Hao, Z. Qu, L.R. Smith, N.F. Dummer, H. Qi, T.J.A. Slater, Z. Zhu, R. Zhang, Z. Sun, Z. Sun, G.J. Hutchings, Ce-induced synergistic effect in exsolved perovskite catalyst for highly efficient and robust methane dry reforming, Nat. Commun. 16 (1) (2025) 10630, https://doi.org/10.1038/s41467-025-65619-w.
[51] A. Garcia-Zaragoza, J.L. del Rio-Rodriguez, C. Cerezo-Navarrete, S. Gutierrez-Tarrino, M.A. Molina, L. Costley-Wood, J. Mazario, B. Chaudret, L.M. Martinez-Prieto, A.M. Beale, P. Ona-Burgos, Pd-enhanced carbon-encapsulated co nanoparticles for efficient reverse water-gas shift under magnetic induction heating, ACS Catal. 15 (11) (2025) 9489–9502, https://doi.org/10.1021/acscatal.5c01232.
[52] I. Mustieles Marin, D. De Masi, L.-M. Lacroix, P.-F. Fazzini, P.W.N.M. van Leeuwen, J.M. Asensio, B. Chaudret, Hydrodeoxygenation and hydrogenolysis of biomass-based materials using FeNi catalysts and magnetic induction, Green Chem. 23 (5) (2021) 2025–2036, https://doi.org/10.1039/d0gc03495a.
[53] J.M. Asensio, A.B. Miguel, P.-F. Fazzini, P.W.N.M. van Leeuwen, B. Chaudret, Hydrodeoxygenation using magnetic induction: high-temperature heterogeneous catalysis in solution, Angew. Chem. Int. Ed. 58 (33) (2019) 11306–11310, https://doi.org/10.1002/anie.201904366.